

Superconducting, Insulating, and Anomalous Metallic Regimes in a Gated Two-Dimensional Semiconductor-Superconductor Array

C. G. L. Böttcher,^{1,*} F. Nichele,¹ M. Kjaergaard,^{1,†} H. J. Suominen,¹
J. Shabani,^{2,‡} C. J. Palmstrøm,^{2,3,4} and C. M. Marcus¹

¹*Center for Quantum Devices and Station Q Copenhagen,
Niels Bohr Institute, University of Copenhagen, 2100 Copenhagen, Denmark*

²*California NanoSystems Institute, University of California, Santa Barbara, CA 93106, USA*

³*Department of Electrical Engineering, University of California, Santa Barbara, CA 93106, USA*

⁴*Materials Department, University of California, Santa Barbara, CA 93106, USA*

(Dated: December 8, 2021)

The superconductor-insulator transition in two dimensions has been widely investigated as a paradigmatic quantum phase transition. The topic remains controversial, however, because many experiments exhibit a metallic regime with saturating low-temperature resistance, at odds with conventional theory. Here, we explore this transition in a novel, highly controllable system, a semiconductor heterostructure with epitaxial Al, patterned to form a regular array of superconducting islands connected by a gateable quantum well. Spanning nine orders of magnitude in resistance, the system exhibits regimes of superconducting, metallic, and insulating behavior, along with signatures of flux commensurability and vortex penetration. An in-plane magnetic field eliminates the metallic regime, restoring the direct superconductor-insulator transition, and improves scaling, while strongly altering the scaling exponent.

As temperature is lowered, two-dimensional (2D) materials may become superconductors, or, if highly disordered or in a strong magnetic field, may become insulators, with resistance diverging with falling temperature. Despite decades of work on this topic [1–5], the question of whether such a system can remain a metal, converging toward a finite resistance at low temperatures, remains unresolved [6].

Within conventional frameworks, the 2D superconductor-insulator transition (SIT) is driven either by phase fluctuations of the superconducting order parameter, leading to localized Cooper pairs, or reduction in the superconducting pairing amplitude due to unscreened repulsive interactions. In either case, theory suggests a direct quantum phase transition between superconductor and insulator as a function of disorder, magnetic field, or carrier density, with no metal phase.

Much of the experimental literature has focussed on the direct SIT, often finding good agreement with scaling theory [4, 7–12]. However, a number of experiments have reported an intervening metallic regime with saturating low-temperature resistance in a variety of systems, including metal films [13, 14], oxides [10, 15], Josephson junction arrays (JJAs) [16], and superconducting islands on graphene, enabling electrostatic gating [17]. Proposed theoretical explanations for the observed metallic behavior include order-parameter fluctuations [18–20], emergence of a Bose metal phase [21–23], coupling to a dissipative bath [7, 24], or a composite Fermi liquid phase [25].

Here, we experimentally investigate the transition from superconductor to insulator in a highly controllable system based on a two-dimensional electron gas (2DEG) formed in a semiconductor heterostructure with an epitaxial Al layer [26]. By depleting carriers between patterned islands of the Al layer with an electrostatic gate, the 2D sheet resistance, R_s , was controlled from below $0.1 \, \Omega$ to above $10^8 \, \Omega$, spanning regimes of global superconductivity to insulating behavior, including a regime with anomalous low-resistance metallic behavior. This system, characterized by high mobility, large g -factor, and strong spin-orbit coupling, along with large in-plane critical magnetic field of the Al islands, opens unexplored territories in condensed matter physics [27, 28], including access to topological superconductivity and its transitions [29].

The heterostructure material consist of a 7 nm InAs quantum well, separated by a 10 nm InGaAs barrier from a 7 nm epitaxial Al layer, grown by molecular beam epitaxy [26], as shown in Fig. 1(a). The Al layer was patterned into a 40×100 array of square islands, each with lateral dimension $a = 1 \, \mu\text{m}$. Two devices, A(B), with spacing $b = 150(350) \, \text{nm}$ between islands [Fig. 1(b)], were measured. The spacing is comparable to the electron mean free path of 300 nm, extracted from measurements on a Hall bar with the Al removed. The structure was covered with 40 nm of Al_2O_3 insulator and a Ti/Au top gate [Fig. 1(c)]. Measurements were made in a dilution refrigerator with a base temperature of 25 mK using standard lock-in techniques. Both the current, I , through the device and the four-terminal voltage, V_{4t} , were directly measured using an AC voltage bias of $5 \, \mu\text{V}$ or less [Fig. 1(c)] [30, 31].

* Now at Harvard University, Cambridge, MA 02138, USA

† Now at MIT, Cambridge, MA 02138, USA

‡ Now at NYU, New York, NY 10003, USA

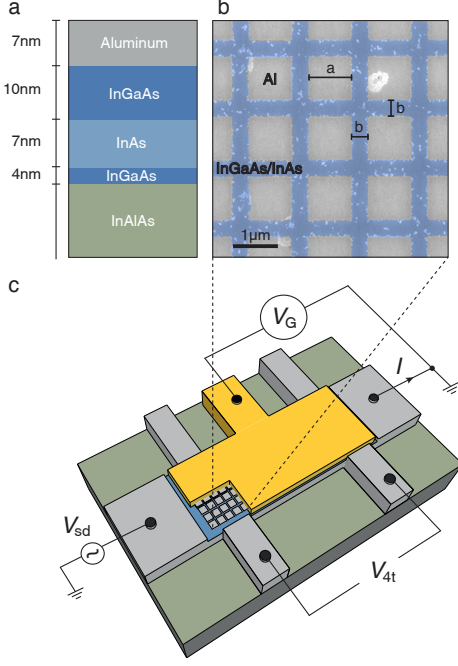


FIG. 1. **Semiconductor/superconductor array.** **a**, InGaAs/InAs heterostructure with epitaxial Al top layer. **b**, Scanning electron micrograph (false color) of device A before deposition of top gate, showing array of square Al islands with lateral dimension $a = 1 \mu\text{m}$ and separation $b = 150 \text{ nm}$. Device B (not shown) has $b = 350 \text{ nm}$. **c**, Device schematic showing current, I , source-drain voltage, V_{SD} , and four-terminal voltage, V_{4t} , measured using side arms of Hall bar.

I. GATE-TUNED TRANSITION AND ANOMALOUS METALLIC REGIME

We use the dependence of R_s on temperature, T , at the lowest measured temperatures to distinguish insulating, metallic, and superconducting regimes. $R_s(T)$ over a range of top-gate voltages, V_G , is shown in Fig. 2(a) for Device A. Device B showed similar behavior (see Supplementary Material). From positive to moderately negative gate voltages, $V_G \gtrsim -3.1 \text{ V}$, R_s was unmeasurably small at the lowest temperatures, and at finite bias showed a critical current of a few μA (see Supplemental Information), indicating a global superconducting state. For more negative gate voltages, $-3.8 \text{ V} \lesssim V_G \lesssim -3.1 \text{ V}$, $R_s(T)$ saturated at the lowest measured temperatures to a gate-voltage-dependent value spanning three orders of magnitude in sheet resistance, from $R_s \sim 1 \Omega$ to $R_s \sim 1 \text{ k}\Omega$, suggesting metallic behavior across this range. For even more negative gate voltages, $V_G \lesssim -3.8 \text{ V}$, $R_s(T)$ increased with decreasing temperature, indicating an insulating regime. At $V_G^* \sim -3.7 \text{ V}$, R_s was roughly independent of temperature, with $R_s^* \sim 10 \text{ k}\Omega$ in this region. Within a conventional SIT framework, this can be identified as the separatrix dividing superconducting and insulating phases. The zero-field critical temperature $T_c \sim 1.6 \text{ K}$ where superconductivity vanishes

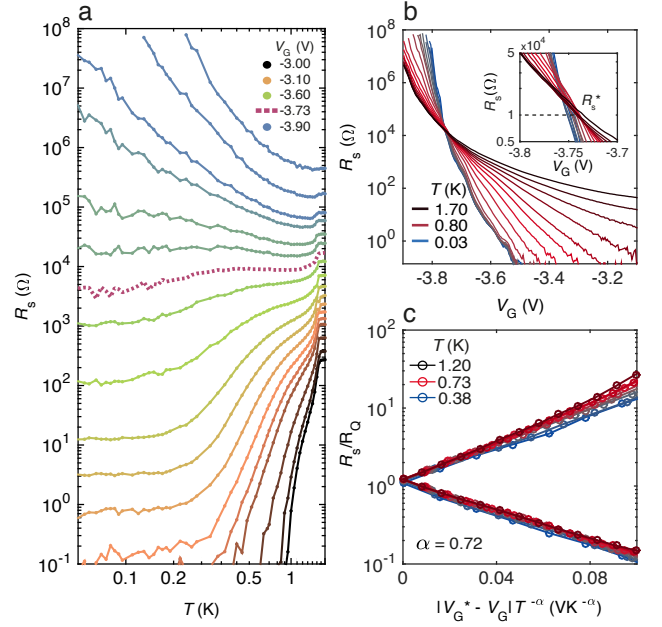


FIG. 2. **Voltage controlled transitions.** **a** Sheet resistance, R_s , as a function of temperature, T , over a range of gate voltages, V_G , from -3.0 V to -3.9 V , spanning the superconducting regime, anomalous metallic regime with saturating R_s at low temperatures, and insulating regime with R_s increasing with lower temperature. The kinks at $\sim 1.6 \text{ K}$ is where superconductivity vanishes in the Al. **b** R_s as a function of V_G for different temperatures reveals an approximate crossing point at $\sim 10 \text{ k}\Omega$. **c** Scaling plot yields best-fit exponent $\alpha = 0.72$, corresponding to $z\nu = 1/\alpha = 1.4$. See text for details.

in the individual islands is visible as a kink at the high-temperature end of Fig. 2(a). As seen in Fig. 2(a)[S4(b)], for Device A[B], the lowest resistance curve that clearly saturates has a normal-state resistance of $\sim 2[6] \text{ k}\Omega$ above $T_c \sim 1.6 \text{ K}$.

Plotting $R_s(V_G)$ for different temperatures yields a near-crossing of all curves around $V_G^* \sim -3.75 \text{ V}$ [Fig. 2(b)]. As seen in the inset of Fig. 2(b), the crossing is smeared over a range spanning $\sim 10 - 20 \text{ k}\Omega$. When restricted to temperatures above saturation, $T \gtrsim 0.3 \text{ K}$, a much improved single crossing point is obtained.

Notwithstanding the metallic (saturating) behavior at low temperatures evident in Fig. 2(a), we perform a scaling analysis of these data within a conventional SIT framework. This will allow comparison to similar data at finite in-plane magnetic field, where the metallic phase vanishes, as discussed below. Scaling theory of the SIT [32] considers a correlation length ξ and correlation time τ , both of which diverge at a critical tuning parameter, in this case gate voltage, with power-law dependences, $\xi \propto (V_G - V_G^*)^{-\nu}$ and $\tau \propto \xi^z \propto (V_G - V_G^*)^{-z\nu}$, yielding a scaling relation for sheet resistance,

$$R_s(V_G, T) = R_s^* F((V_G - V_G^*)T^{-1/z\nu}). \quad (1)$$

with a scaling function $F(x)$ that depends on distance

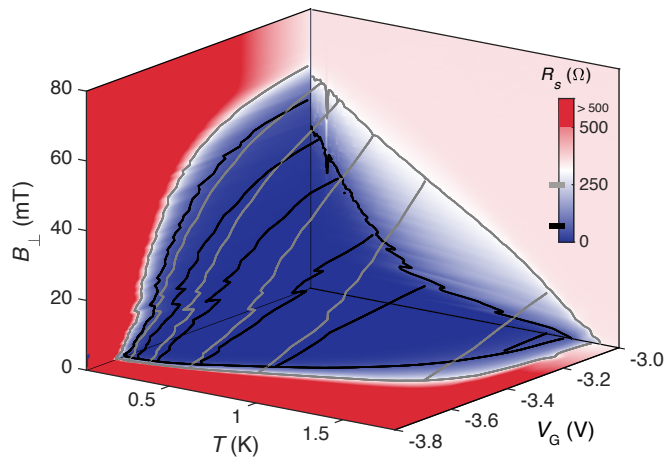


FIG. 3. **Experimental phase diagram.** Three-dimensional phase-diagram-like plot of sheet resistance, R_s (color scale), as a function of temperature, T , perpendicular magnetic field, B_\perp , and gate voltage, V_G . Contours at 50 Ω (black) roughly mark the boundary between superconducting (S) and anomalous metal (M^*) regimes. Contours at 250 Ω (gray) mark the critical field, B_{c2} , between anomalous (M^*) and normal metal (M) regimes in the $V_G = -3.0$ V plane (back wall of diagram). Effects of a fourth control parameter, in-plane magnetic field, are shown in Fig. 6.

from the critical gate voltage, V_G^* , temperature, T , and the product of scaling exponents, $z\nu$.

Experimentally, we plot $R_s(V_G, T)$ as a function of $(V_G - V_G^*)T^{-\alpha}$, treating V_G^* and α as fit parameters optimized to yield the best collapse of data across a range of temperatures and gate voltages. An alternative procedure [10, 13] for extracting α from the temperature dependence of slopes $\partial R_s / \partial V_G$ at the critical point yielded consistent values (see Supplemental Material). Figure 2(c) shows $R_s(V_G, T)$ in units of $R_Q \equiv h/4e^2$, demonstrating good scaling for $T \gtrsim 0.2$ K, covering four orders of magnitude of sheet resistance [Fig. 2(c)], with a best fit exponent $\alpha = 0.72$, corresponding to $z\nu = 1.4$. Experimental scaling exponents are usually compared to theory based on classical percolation ($z\nu = 4/3$) or quantum percolation ($z\nu \sim 2.3$) [10, 12, 14, 15, 33]. The value we find is close to the classical percolation value, similar to what was found in a relatively clean disordered system [15], where an intervening metallic regime was also observed. In that study, it was found that increasing disorder yielded a direct SIT with $R_s^* \sim R_Q$ and $z\nu \sim 2.3$, consistent with quantum percolation.

II. PHASE DIAGRAM

Motivated by the theoretical phase diagram for the dirty boson model of the SIT [32], we show R_s as a function of T , V_G , and perpendicular magnetic field, B_\perp , yielding the phase-diagram-like plot in Fig. 3. Rather than phase boundaries, the lines in Fig. 3 are contours of

R_s , with the 50 Ω contour roughly marking the boundary between superconducting (S) and anomalous metallic (M^*) regimes, and the 250 Ω contour marking the critical magnetic field $B_{c2}^\perp(V_G, T)$ to the normal metallic (M) regime for $V_G = -3.0$ V, above which R_s is independent of temperature and field. The existence of two distinct crossovers in the B_\perp - T plane is a robust experimental feature, investigated in detail below.

Plots of R_s in three B_\perp - T planes are shown in Fig. 4, along with current-voltage (I - V) curves taken at indicated points in each of the planes. The plane in Fig. 4(a) at $V_G = -3.0$ V is the same as the back wall of Fig. 3. A dashed curve in Fig. 4(a), repeated in Figs. 4(b) and 4(c), shows the boundary of M and M^* regions. The boundary is clearly visible in the data in Fig. 4(a), less so in the other B_\perp - T planes. At moderately negative gate voltages [Fig. 4(b)], the boundary to the superconducting regime is reentrant, with a dip around $T \sim 0.5$ K. In the vicinity of this dip, two field-driven transitions are observed, an S-I transition on the low-temperature side and an S-M transition at higher temperatures. The boundary between these regimes, shown as a vertical dashed line in Fig. 4(b), is not visible in R_s but can be seen in the nonlinear I - V curves, described below. At more negative gate voltages [(Fig. 4(c))] an insulating regime emerges at low temperatures, with resistance that first rises with B_\perp then falls, similar to behavior in InO films [34].

Further characteristics of the superconducting, insulating, anomalous metal, and normal metal regimes can be found in nonlinear transport. Differential resistance dV/dI as a function of applied dc current I_{DC} is shown in Figs. 4(d-i), with the corresponding point where the measurement was taken indicated in the B_\perp - T cuts, Figs. 4(a-c). Along the left axis of Fig. 4a ($T = 30$ mK), superconductivity was observed at small current bias, with a critical current of $I_c \sim 20 \mu\text{A}$ at zero field (Fig. 4d). Moving upward to $B_\perp = 60$ mT, superconductivity is lost, and normal metal (M) behavior observed, with R_s independent of T and B_\perp , and flat dV/dI . At intermediate fields, the M^* regime in Fig. 4(a), dV/dI retains a dip around zero current, suggesting some vestige of superconductivity but not a zero resistance state. Moving to $T = 800$ mK (Fig. 4e), the sampling of dV/dI curves straddle the M^* -M boundary: In the M^* regime at $B_\perp = 25$ mT, dV/dI showed a dip saturating at a nonzero value; In the M regime at $B_\perp = 40$ mT, dV/dI was flat.

Nonlinear transport at more negative gate voltages [Fig. 4(f)], crossing from M^* to I, showed a zero-bias dip in dV/dI at low field (M^*) and temperature, crossing to a zero-bias peak in dV/dI at higher field (I). At the B_\perp -driven M^* -I crossover, $R_s^* \sim 10 \text{ k}\Omega$, consistent with the T -driven crossover described above [Fig. 2]. At temperatures above the reentrant feature around 0.5 K in Fig. 4(b), the peak in dV/dI vanished, indicating a normal metallic (M) regime [Fig. 4(g)]. The vertical separation line in Fig. 4(b) is based on the vanishing peak in dV/dI , not by features in R_s .

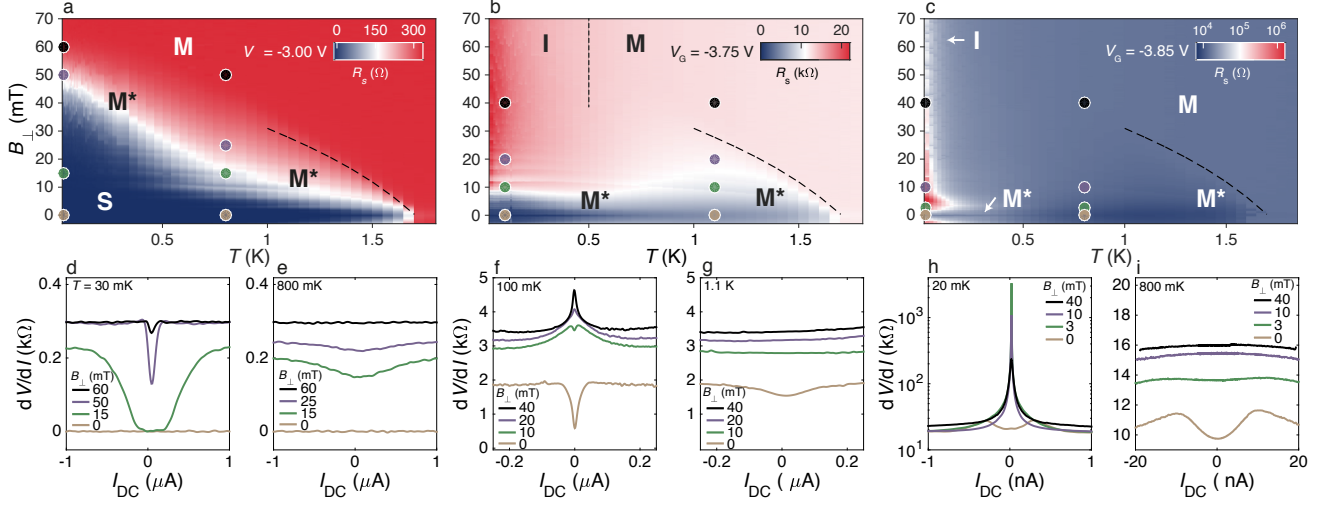


FIG. 4. **Temperature, magnetic field, and nonlinear response.** **a** Sheet resistance R_s (color scale) in the $T - B_{\perp}$ plane at the least negative gate voltage, $V_G = -3.00$ V shows superconducting (S), anomalous (M^*) and normal (M) metal regimes. Boundaries between S and M^* (white data) and between M^* and M (dashed curve, determined by flat versus dipped dV/dI). The same dashed curve is also plotted **b** and **c**. **b** R_s (color scale) at intermediate gate voltage, $V_G = -3.75$ V. M^* and I regimes determined from temperature dependence; M regime determined from the flat dV/dI curves. Position of vertical dashed line separating I and M based on dV/dI curves. Note the reentrant dip in the M^* regime around 0.5 K. **c** R_s (color scale) at more negative gate voltage, $V_G = -3.85$ V. M^* shows a giant peak in R_s as a function of B_{\perp} , along with a narrow zero-bias peak in dV/dI at 20 mK. The M^* regime defined by temperature saturation, also associated with zero-bias dip in dV/dI . **d-i** Differential resistance dV/dI as a function of applied current bias, I_{DC} , at values of T , B_{\perp} , indicted by colored circles in **a-c**.

As the gate voltage is tuned farther negative, [Fig. 4(c)], the system exhibits strong insulating behavior at low temperature and magnetic field, with an associated giant zero-bias peak in dV/dI as a function of field, spanning several orders of magnitude in resistance [Fig. 4(h)], as reported previously [9, 15, 34] and discussed in detail below. At elevated temperatures, $T > 800$ mK, R_s decreases, as expected in the insulating regime. At low fields, the zero-bias peak in dV/dI seen at low temperature crosses over to a zero-bias dip, consistent with an M^* regime, as temperature is raised. Note that $R_s > 10$ k Ω , despite the zero-bias dip (Fig. 4i).

Transport in the weakly insulating regime is well described by Efros-Shklovskii variable range hopping, $R(T) \propto \exp(T_1/T)^{1/2}$ [35], as seen previously, for instance, in TiN films [36]. Fits yield $T_1 \sim 2.5$ K, consistent with the theoretical prediction, $T_{ES} = 2.8(1/4\pi\epsilon'\epsilon_0)(e^2/k_B\xi) \sim 3$ K, where ξ is the coherence length and ϵ' is the material dielectric constant [35, 37]. At the most negative gate voltages, transport crosses over to an activated form, $R(T) \propto \exp(T_0/T)$. Fits yield $T_0 \sim 1.5$ K, comparable to the zero-field T_c , a relation previously observed in disordered InO films [38]. Data for variable range hopping and activated transport are presented in the Supplementary Material.

III. FLUX EFFECTS

We next investigate flux effects at low fields, both commensuration features associated with the periodic array, and flux penetration of individual Al islands. Both are evident in the three panels of Fig. 5, measured at different gate voltages. In Fig. 5(a), the features labeled $f = 1 \dots 4$ indicate numbers of flux quanta per area of the periodic array, $f = B_{\perp}/B_0$, where $B_0 = \Phi_0/A$ with A being the area of a unit cell [$A = (a+b)^2$] and $\Phi_0 = h/2e$ is the superconducting flux quantum. From the device design, $B_0 = 1.8$ mT, consistent with the positions of these features. At integer values of f , there is a dip in R_s , which at the lowest temperatures extends into the superconducting state. Dips in R_s at fractional values of f , most prominently at $f = 1/2$, are also observed. Similar features are commonly observed in regular Josephson arrays [39]. All panels in Fig. 5 are marked on their top axis with the positions of these features. They are most pronounced in Fig. 5(a), where superconductivity persists, and are essentially absent in the insulating regime [Fig. 5(c)]. Commensuration dips at integer and fractional f values become less pronounced as the temperature is raised, but do not move in field with temperature. In contrast, the positions of a second set of features in R_s , labeled $n = 1 \dots 3$ in Fig. 5(a), are strongly temperature dependent. We associate this second set of features with vortex penetration of the individual Al islands, in good agreement with previous studies on single micron-size Al squares [40].

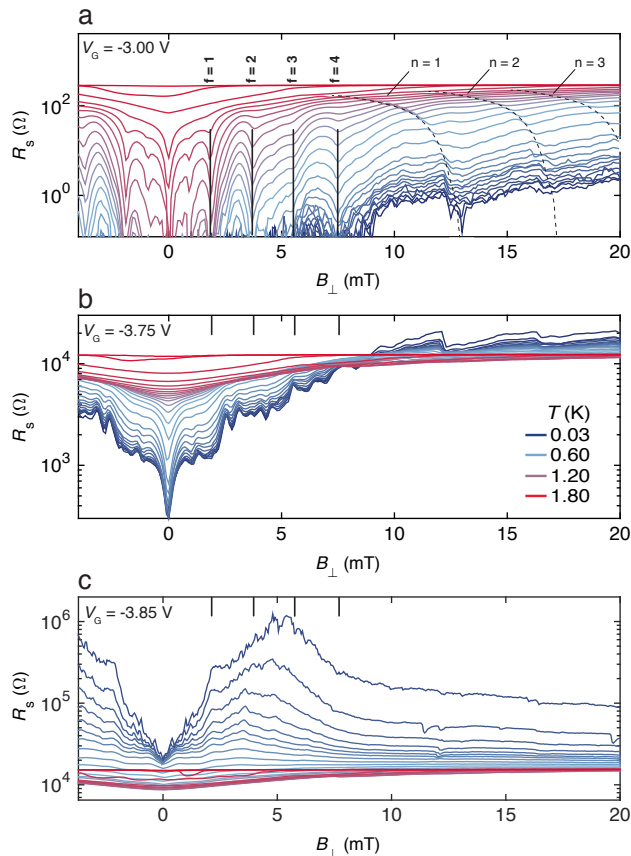


FIG. 5. **Flux effects in S, M*, and I regimes.** **a** Sheet resistance, R_s , in the superconducting regime, $V_G = -3.00$ V. Flux commensuration effects for $f = 1...4$ flux quanta per unit cell of the array were independent of temperature (marked with vertical lines). Dips at fractional values $f = 1/3, 1/2$ are also visible. Flux penetration into the Al islands for $n = 1...3$ flux quanta per island occur at fields that depend strongly on temperature. Legend for temperatures are given in **b**. **b** At intermediate gate voltage, $V_G = -3.75$ V, low-temperature saturation of R_s —the defining characteristic of the M* regime—is seen as an accumulation of curves at low-temperature. Saturation resistance shows mesoscopic fluctuations on a field scale smaller than one flux quantum per unit cell, with a large dip at zero field. At higher fields, the low-temperature curves exceed the high temperature curves above ~ 10 mT, indicating a crossover to the insulating regime. **c** At more negative gate voltage, $V_G = -3.85$ V, in the insulating regime, a giant peak in R_s appears around a few times $B_0 = \Phi_0/A$, with some plateau structure at $B \sim B_0$ ($f \sim 1$). Legend for temperatures are given in **b**.

Novel flux effects were observed in the M* regime, where R_s decreases with decreasing temperature then saturates [Fig. 5(b)]. Three features in the data are notable: (i) The low-temperature saturation value of R_s depends sensitively on magnetic field, showing mesoscopic fluctuations on a field scale smaller than B_0 , with symmetric saturation values at positive and negative fields, and an absence of hysteresis that one might have anticipated for flux trapping. (ii) The saturation value of R_s

showed a deep minimum at $B_\perp = 0$, the time-reversal symmetric situation. The field scale for the dip is less than 1 mT, smaller than B_0 , suggesting that this feature is due to coherence among many islands. (iii) The saturation value of R_s ranges over two orders of magnitude, controlled by field, at fixed gate voltage. Lacking an understanding of the M* regime and the mechanism leading to saturation, we do not put forward a model of mesoscopic fluctuations and antilocalization of the saturation of R_s .

The insulating regime [Fig. 5(c)] showed a giant peak in R_s at roughly the B_0 field scale, with a peak rising by nearly two orders of magnitude in a field of 5 mT at the lowest temperature. Similar effects have been reported in other SIT systems [9, 15, 38]. The field scale suggests that phase disorder in the array is responsible for the high resistance. A plateau-like feature at ~ 2 mT, seen over a range of temperatures, appears correlated with $f = 1$ flux commensuration.

IV. IN-PLANE MAGNETIC FIELD EFFECTS

Because the epitaxial Al layer is thin (7 nm), the critical in-plane field is large, typically around 2 T [26]. However, due to both the finite thickness of the heterostructure and the large g -factor of InAs, global superconductivity in the arrays was found to vanish above a critical in-plane field $B_\parallel^* = 0.6$ T. We investigate effects of B_\parallel , oriented along the current direction, for Device B. An example for $B_\parallel = 275$ mT is shown in Fig. 6, with additional data in the Supplemental Material. We found that the in-plane magnetic field largely suppresses the M* regime, leaving only a single separatrix moving horizontally throughout the temperature range, including the lowest temperatures. We speculate that the softening of the proximity-induced gap by the in-plane field [31] quenched the coherence intrinsic to the anomalous metal regime, noting inconsistency with Ref. 24, which argued that dissipation stabilized the anomalous metal. Repeating the SIT scaling analysis, now in the absence of the intervening saturating curves, yields a single crossing point [Fig. 6(b)] of curves and better collapse of data [Fig. 6(c)]. We observed an unexplained systematic reduction of α with increasing B_\parallel , by over an order of magnitude, while the crossing point, R_s^* , does not vary systematically [Fig. 6(b), inset]. Dependence of α on B_\parallel is not understood, but may also result from dissipation due to the softening of the gap [41].

V. SUMMARY AND DISCUSSION

The ability to repeatedly and accurately control the crossover from superconducting to insulating behavior using a gate voltage enables new ways of investigating the SIT and the long-debated anomalous metal

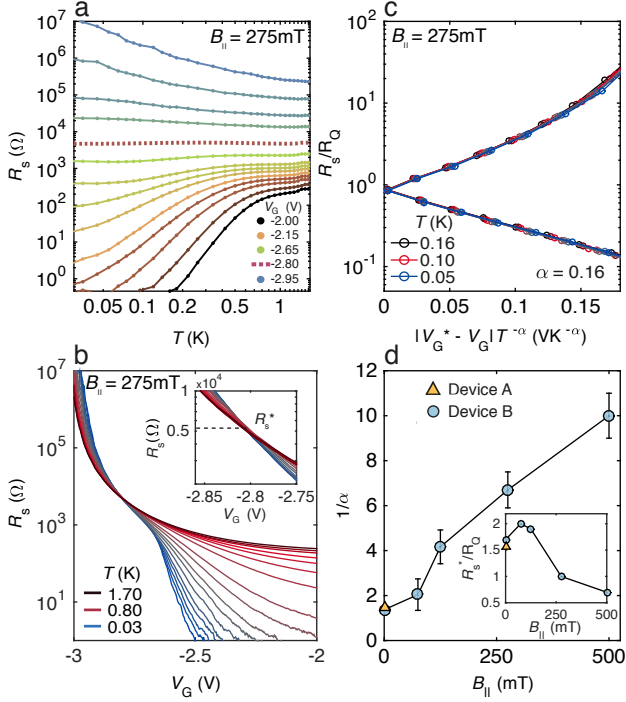


FIG. 6. **In-plane magnetic field effects.** Gate-tuned SIT at $B_{||} = 275$ mT. **a** Sheet resistance, R_s , as a function of T and gate voltage V_G . Separatrix at $V_G = -2.80$ V (dashed curve) corresponds to the intersection of curves in **b**. **b** R_s as a function of gate voltage for several temperatures, shows very accurate single crossing point. Inset: Crossing point value of sheet resistance, R_s^* , for several in-plane field values of device A (triangle) and B (circles) shows no clear trend. **c** Scaling plot (see text) for $B_{||} = 275$ mT shows excellent collapse with a single critical exponent $\alpha = 0.16$. **d** Critical exponent for device A (triangle, only at zero field) and B (circle) shows a clear trend of increasing $1/\alpha$ with $B_{||}$.

state. A novel physical system comprising epitaxially grown semiconductor-superconductor heterostructures that makes these investigations relatively straightforward experimentally. In the present study, the device geometry itself is simple; we have not yet considered the wealth of new device geometries that become possible using range of materials and arbitrary lithographic patterning. The thinness of the epitaxial superconductor also makes in-plane field studies readily accessible, opening the door, for instance, to topological superconductivity [29] and its transitions. Several observations reported here in these initial experiments are familiar from the SIT [4, 5] and JJ-array [42] literature; some observations are new, accessible for the first time.

Besides the observed scaling in the vicinity of the critical R_s , yielding a scaling exponent $z\nu \sim 1.4$, and a phase-diagram-like plot of R_s in the space of T , B_{\perp} , and V_G , we observed an anomalous metallic regime, with saturating sheet resistance at low temperature, resembling similar behavior reported previously in a variety of systems [7, 12, 15–17, 43]. New observations concerning

the metallic regime include mesoscopic fluctuations of the saturating resistance and a strong reduction in the saturation resistance at $B = 0$, on a field scale significantly smaller than one flux quantum per period of the array. The absence of an anomalous metallic regime in an in-plane magnetic field indicates that it is unlikely that uncontrolled heating is responsible for the saturation. The striking dependence of the scaling exponent on in-plane field remains unexplained, but may result from dissipation [41] due to a softened gap [31].

VI. METHODS

The wafer structure was grown by molecular beam epitaxy to obtain 7 nm InAs quantum well with a 10 nm InGaAs upper barrier and 7 nm of Al grown *in situ*. The epitaxial grown Al results in a pristine superconductor/semiconductor interface [26] and hard induced gap in the semiconductor [31].

The devices were fabricated with first electron beam lithography to define the mesas with a Hall-bar geometry and etched using a wet etch solution of $\text{H}_2\text{O} : \text{citric acid} : \text{H}_3\text{PO}_4 : \text{H}_2\text{O}_2$ in the ratio 220 : 55 : 3 : 3. The Al layer on each mesa was then selectively etched using Transene type-D to pattern it into a 40×100 array of square islands [30, 31]. The results reported here are performed on Device A(B), with island dimension of 1 μm and spacing between the islands was 150(350) nm. Atomic layer deposition of 40 nm Al_2O_3 was used to form a dielectric between the well-defined Al square array and a Ti/Au (10/200 nm) top gate. Wire bonding to the epitaxial Al formed low resistance Ohmic contacts.

A separate Hall bar with all Al removed was used to characterize the 2DEG and partially depleted to enter a density regime with a single subband occupied, reached at a gate voltage value $V_G \sim -2$ V. Results yielding a maximum mobility of $\mu = 20,000 \text{ cm}^2\text{V}^{-1}\text{s}^{-1}$ at a sheet density of $n_e = 1 \times 10^{12} \text{ cm}^{-2}$, corresponding to a mean free path $l_e = 300$ nm, comparable to the separation between islands. In addition, the epitaxial Al film has been characterized, yielding a superconducting transition temperature $T_c = 1.5$ K. In-plane and out-of-plane critical field values were measured to be $B_{||,c} \sim 1.6$ T and $B_{\perp,c} \sim 30$ mT respectively [44].

Measurements were carried out in a dilution refrigerator with a base temperature of 25 mK. The four-terminal voltage, V_{4t} , and current, I , through the device were directly measured with AC voltage bias in all cases kept below 5 μV , using standard low frequency lock-in techniques. Series resistance in the lines were in the range of a few kilohms, creating an effective current bias in the low-resistance regime and voltage bias in the high-resistance regime.

In-plane field was precisely aligned with the plane of the array using a three-axis vector magnet by maximizing the critical current while trimming out-of-plane field coils.

Acknowledgements: We thanks A. Kapitulnik, S. Kivelson, D. Shahar, B. Spivak, C. Strunk, and V. Vinokur for useful discussion. Research was supported by Microsoft Station Q and the Danish National Research

Foundation. C.M.M. acknowledges support from the Villum Foundation. F.N. acknowledges support from a Marie Curie Fellowship (no. 659653).

-
- [1] Jaeger, H. M., Haviland, D. B., Orr, B. G. & Goldman, A. M. Onset of superconductivity in ultrathin granular metal films. *Phys. Rev. B* **40**, 182–196 (1989).
 - [2] Lee, S. J. & Ketterson, J. B. Critical sheet resistance for the suppression of superconductivity in thin Mo-C films. *Phys. Rev. Lett.* **64**, 3078–3081 (1990).
 - [3] Goldman, A. M. Superconductor-Insulator Transitions. *International Journal of Modern Physics B* **24**, 4081–4101 (2010).
 - [4] Gantmakher, V. F. & Dolgoplov, V. T. Superconductor-insulator quantum phase transition. *Physics-Uspekhi* **53**, 1 (2010).
 - [5] Dobrosavljevic, V., Trivedi, N. & Jr, J. M. V. *Conductor Insulator Quantum Phase Transitions*, vol. 1 (Oxford University Press, United Kingdom, 2012).
 - [6] Kapitulnik, A., Kivelson, S. A. & Spivak, B. Anomalous Metals – Failed Superconductors. *Rev. Mod. Phys.* (in preparation).
 - [7] Mason, N. & Kapitulnik, A. Dissipation effects on the superconductor-insulator transition in 2D superconductors. *Phys. Rev. Lett.* **82**, 5341–5344 (1999).
 - [8] Yazdani, A. & Kapitulnik, A. Superconducting-insulating transition in two-dimensional *a*-MoGe thin films. *Phys. Rev. Lett.* **74**, 3037–3040 (1995).
 - [9] Steiner, M. & Kapitulnik, A. Superconductivity in the insulating phase above the field-tuned superconductor-insulator transition in disordered indium oxide films. *Physica C* **422**, 16–26 (2005).
 - [10] Bollinger, A. T. *et al.* Superconductor-insulator transition in $\text{La}_{2-x}\text{Sr}_x\text{CuO}_4$ at the pair quantum resistance. *Nature* **472**, 458–460 (2011).
 - [11] Schneider, R., Zaitsev, A. G., Fuchs, D. & v. Löhneysen, H. Superconductor-insulator quantum phase transition in disordered FeSe thin films. *Phys. Rev. Lett.* **108**, 257003 (2012).
 - [12] Allain, A., Han, Z. & Bouchiat, V. Electrical control of the superconducting-to-insulating transition in graphene-metal hybrids. *Nat. Mater.* **11**, 590–594 (2012).
 - [13] Marković, N., Christiansen, C., Mack, A. M., Huber, W. H. & Goldman, A. M. Superconductor-insulator transition in two dimensions. *Phys. Rev. B* **60**, 4320–4328 (1999).
 - [14] Park, S., Shin, J. & Kim, E. Scaling analysis of field-tuned superconductor-insulator transition in two-dimensional tantalum thin films. *Sci. Rep.* **7**, 42969 (2017).
 - [15] Steiner, M. A., Breznay, N. P. & Kapitulnik, A. Approach to a superconductor-to-Bose-insulator transition in disordered films. *Phys. Rev. B* **77**, 212501 (2008).
 - [16] Eley, S., Gopalakrishnan, S., Goldbart, P. M. & Mason, N. Approaching zero-temperature metallic states in mesoscopic superconductor-normal-superconductor arrays. *Nat. Phys.* **8**, 59–62 (2012).
 - [17] Han, Z. *et al.* Collapse of superconductivity in a hybrid tin-graphene Josephson junction array. *Nat. Phys.* **10**, 380–386 (2014).
 - [18] Feigel'man, M. & Larkin, A. Quantum superconductor-metal transition in a 2d proximity-coupled array. *Chemical Physics* **235**, 107 – 114 (1998).
 - [19] Spivak, B., Zyuzin, A. & Hruska, M. Quantum superconductor-metal transition. *Phys. Rev. B* **64**, 132502 (2001).
 - [20] Spivak, B., Oreto, P. & Kivelson, S. A. Theory of quantum metal to superconductor transitions in highly conducting systems. *Physical Review B* **77**, 214523 (2008).
 - [21] Lee, D.-H., Kivelson, S. & Zhang, S.-C. Theory of the quantum-Hall liquid to insulator transition. *Phys. Rev. Lett.* **67**, 3302–3305 (1991).
 - [22] Kivelson, S., Lee, D.-H. & Zhang, S.-C. Global phase diagram in the quantum Hall effect. *Phys. Rev. B* **46**, 2223–2238 (1992).
 - [23] Phillips, P. & Dalidovich, D. The elusive Bose metal. *Science* **302**, 243–247 (2003).
 - [24] Kapitulnik, A., Mason, N., Kivelson, S. A. & Chakravarty, S. Effects of dissipation on quantum phase transitions. *Physical Review B* **63**, 125322 (2001).
 - [25] Mulligan, M. & Raghu, S. Composite fermions and the field-tuned superconductor-insulator transition. *Phys. Rev. B* **93**, 205116 (2016).
 - [26] Shabani, J. *et al.* Two-dimensional epitaxial superconductor-semiconductor heterostructures: A platform for topological superconducting networks. *Phys. Rev. B* **93**, 155402 (2016).
 - [27] Chalker, J. T. *et al.* Thermal metal in network models of a disordered two-dimensional superconductor. *Physical Review B* **65**, 012506 (2001).
 - [28] Dimitrova, O. & Feigel'man, M. V. Theory of a two-dimensional superconductor with broken inversion symmetry. *Phys. Rev. B* **76**, 014522 (2007).
 - [29] Levine, Y., Haim, A. & Oreg, Y. Realizing topological superconductivity with superlattices. *ArXiv* (2017). 1707.08130.
 - [30] Chang, W. *et al.* Hard gap in epitaxial semiconductor-superconductor nanowires. *Nat. Nanotechnol.* **10**, 232–236 (2015).
 - [31] Kjaergaard, M. *et al.* Quantized conductance doubling and hard gap in a two-dimensional semiconductor-superconductor heterostructure. *Nat. Commun.* **7**, 12841 (2016).
 - [32] Fisher, M. P. A. Quantum phase transitions in disordered two-dimensional superconductors. *Phys. Rev. Lett.* **65**, 923–926 (1990).
 - [33] Biscaras, J. *et al.* Multiple quantum criticality in a two-dimensional superconductor. *Nat. Mater.* **12**, 542–548 (2013).
 - [34] Breznay, N. P., Steiner, M. A., Kivelson, S. A. & Kapitulnik, A. Phase transition in granulated superconductors. *PNAS* **113**, 208–285 (2016).
 - [35] Shklovskii, B. I. & Efros, A. L. *Electronic Properties of Doped Semiconductors* (Springer, Berlin, 1984).

- [36] Baturina, T. I., Mironov, A. Y., Vinokur, V. M., Baklanov, M. R. & Strunk, C. Localized Superconductivity in the Quantum-Critical Region of the Disorder-Driven Superconductor-Insulator Transition in TiN Thin Films. *Phys. Rev. Lett.* **99**, 39 (2007).
- [37] Joung, D. & Khondaker, S. I. Efros-Shklovskii variable-range hopping in reduced graphene oxide sheets of varying carbon sp² fraction. *Physical Review B* **86**, 1964–8 (2012).
- [38] Sambandamurthy, G., Engel, L. W., Johansson, A. & Shahar, D. Superconductivity-related insulating behavior. *Phys. Rev. Lett.* **92**, 107005 (2004).
- [39] Fazio, R. & van der Zant, H. Quantum phase transitions and vortex dynamics in superconducting networks. *Physics Reports* **355**, 235 – 334 (2001).
- [40] Baelus, B. J. *et al.* Multivortex and giant vortex states near the expulsion and penetration fields in thin mesoscopic superconducting squares. *Phys. Rev. B* **73**, 024514 (2006).
- [41] Wagenblast, K. H., van Otterlo, A., Schön, G. & Zimanyi, G. T. New universality class at the superconductor-insulator transition. *Phys. Rev. Lett.* **78**, 1779–1782 (1997).
- [42] van der Zant, H. S. J., Elion, W. J., Geerligs, L. J. & Mooij, J. E. Quantum phase transitions in two dimensions: Experiments in Josephson-junction arrays. *Phys. Rev. B* **54**, 10081–10093 (1996).
- [43] Couëdo, F. *et al.* Dissipative phases across the superconductor-to-insulator transition. *Sci. Rep.* **6**, 35834 (2016).
- [44] Suominen, H. J. *et al.* Anomalous fraunhofer interference in epitaxial superconductor-semiconductor josephson junctions. *Phys. Rev. B* **95**, 035307 (2017).
- [45] Shi, X., Lin, P. V., Sasagawa, T., Dobrosavljević, V. & Popović, D. Two-stage magnetic-field-tuned superconductor-insulator transition in underdoped La_{2-x}Sr_xCuO₄. *Nature Physics* **10**, 437–443 (2014).
- [46] Orlando, T. P., Mooij, J. E. & van der Zant, H. S. J. Phenomenological model of vortex dynamics in arrays of Josephson junctions. *Phy. Rev. B* **43**, 10218–10228 (1991).

VII. SUPPLEMENTARY MATERIAL

A. Scaling analysis

The experimental scaling exponent, α , used to collapse data in Figs. 2(c) and 5(c) of the main text, corresponds to $1/z\nu$ for the dirty-boson scaling theory of the superconductor-insulator transition (SIT) [32], where ν describes scaling of correlation length and z of correlation time, as discussed in the main text. The value of α was determined both by optimizing the collapse of the data and, following Ref. 45, by numerically differentiating $R_s(V_G)$ in the vicinity of the critical gate voltage, V_G^* , where curves at different temperatures cross at the critical sheet resistance R_s^* (see Figs. 2(b) and 5(b) in the main text).

Fitting a line to the log of the absolute value of the derivative at the critical point, $|\partial R_s(T, V_G)/\partial V_G|_{V_G=V_G^*}$, as a function of temperature, T , yields a value for α as the slope of that best-fit line,

$$\log |\partial R_s(T, V_G)/\partial V_G|_{V_G=V_G^*} = \log |R_s^* F'(0)| - \alpha \log(T). \quad (2)$$

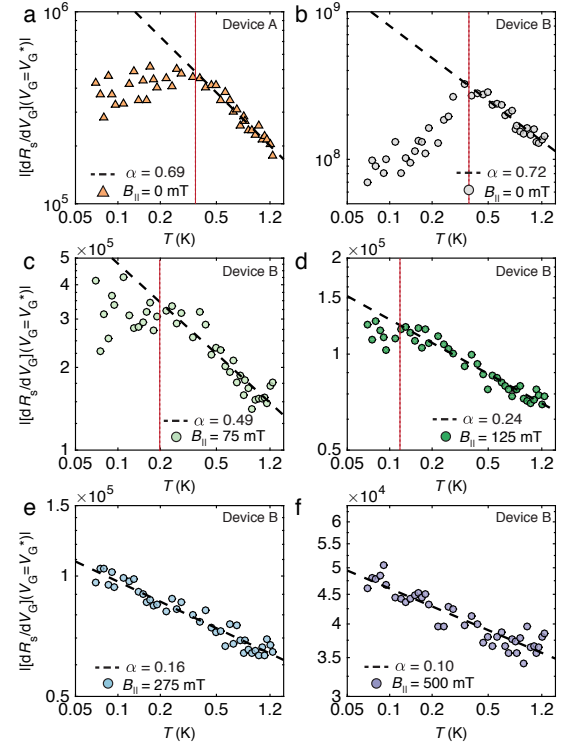


FIG. S1. **Scaling analysis** Dependence on temperature, T , of the slope of sheet resistance, R_s , as a function of gate voltage, V_G , yields an estimate for the scaling exponent, α . Note that scaling only works above a certain temperature (red dotted line), which decreases as an in-plane magnetic field, $B_{||}$ is added, eventually covering the full temperature range of the measurement. The deviation from scaling presumably reflects the appearance of the anomalous metallic phase, M^* . Resulting values for α are plotted as a function of $B_{||}$ in Fig. 6(d) of the main text.

Data and best-fit lines are shown in Fig. S1 for several values of in-plane magnetic field ranging from $B_{\parallel} = 0$ to $B_{\parallel} = 0.5$ T. For $B_{\parallel} = 0$ in both devices, data at higher temperatures are well described by the line fit, while at lower temperatures, the data deviates significantly, associated with the onset of the anomalous metallic regime (M^*). In these cases, the value of α was determined by fitting the data above crossover temperature, out of the M^* regime, where the fit is good, marked as a vertical dotted line in Fig. S1. Figures S1(c-f) demonstrate how the application of B_{\parallel} shrinks the M^* regime, extending the temperature range where scaling works well to the lowest measured temperatures.

B. Comparing superconducting, anomalous metallic, and insulating regimes for Devices A and B

The three T - B_{\perp} planes in Fig. 4 of the main text show S, M^* , and I regimes at low temperature and field, and a normal metallic (M) behavior at high temperature and field. These plots, for Device A, are shown again in Fig. S2 without marked boundaries or labels, along with corresponding data for Device B. Gate voltages for Device B were set so that its normal-state resistance matched the normal-state resistance of Device A in each of the planes. Behavior of Device A and Device B are similar, despite the difference in island space in the two devices ($b_A = 150$ nm, $b_B = 350$ nm).

Dashed curves in Fig. 4 (main text) indicating the crossover from M and M^* , can now be more readily seen a contrast in the data in Fig. S2(a), which is the same data as Fig. 4(a), with no curve added. The curve Fig. 4(a) is a fourth order polynomial fit to the contrast feature. The corresponding curves are less visible in Figs. S2(b,c). The gate voltages for Device A are the same as shown in Fig. 4.

C. Current bias dependence: critical currents separating zero-resistance, flux-flow, and normal-state transport

Figure 4(d) of the main text shows a zero-resistance state at zero magnetic field in the range of ± 1 μ A current bias. On an expanded range, two transitions to resistive states were observed, defining two critical currents, as shown in Fig. S4 for Device A for $V_G = -3.00$ V. Below the first transition, dV/dI was unmeasurably small, suggesting global superconductivity, corresponding to the zero-field data in Fig. 4(d) of the main text.

As seen in Fig. S3(b), a first transition occurred at ~ 5 μ A into a finite-resistance state. In this state, the voltage increased roughly in proportion to the applied current bias. That is, the normalized differential resistance dV/dI was roughly constant. Normalization of dV/dI is done by multiplying by $W/L = 0.32$, where W is the width of the Hall bar and L is the distance be-

tween voltage probes. With this normalization, dV/dI is a differential *sheet* resistance, corresponding to R_s for the case of zero bias. As seen in Fig. S3(b), at ~ 20 μ A a second transition was observed to a state with larger differential sheet resistance, dV/dI . The value of dV/dI above the second transition is equal to R_s in the normal metallic (M) regime. We associate the lower- dV/dI state with the flux-flow regime [46], noting the increasing dV/dI with increasing B_{\perp} , characteristic of flux-flow resistance. Both critical currents depend on magnetic field, the higher one decreasing roughly linearly with B_{\perp} , as seen in Fig. S3(a).

D. Full data sets with in-plane magnetic field

Application of an in-plane magnetic field, B_{\parallel} , reduces the crossover temperature to the anomalous metallic (M^*) regime, where scaling fails [see Fig. S1] and sheet resistance $R_s(T)$ saturates. In-plane field improves the overall quality of scaling and lowers the scaling exponent, α . In the main text, these trends are presented in Fig. 6. Figure S4 shows full data sets of $R_s(T, V_G)$ at different values of B_{\parallel} . Devices A and B are shown at $B_{\parallel} = 0$. For other values of B_{\parallel} , Device B is shown.

E. Insulating regime: activated transport and variable range hopping

We characterize transport on the insulating side of the gate-tuned SIT [Fig. S5(a)] by constructing two plots that each displays the temperature dependence of the resistance. Deep in the insulating regime, roughly from $V_G = -3.85$ V to -3.90 V the resistance show activated behavior, $R(T) \propto \exp(T_0/T)$, and follows a straight line on Arrhenius plot [Fig. S5(b)]. At lower resistances but still in the insulating regime, transport does not look activated; the three lower curves in Fig. S5(b) appear curved. Instead, in the weakly insulating regime near the separatrix, transport appears well described by Efros-Shklovskii variable range hopping (ES-VRH), $R(T) \propto \exp(T_1/T)^{1/2}$ [35]. This can be seen in Fig. S5(c), where the lower three curves appear as straight lines when R_s plotted on a log vertical scale against $T^{-1/2}$. The existence of a smooth crossover from ES-VRH to activation suggests that the insulating regime is first accompanied by a suppression of the density of states around zero energy due to Coulomb interactions, which at more negative gate voltages becomes a Coulomb gap. For ES-VRH, fits in Fig. S5(c) give $T_1 \sim 2.3 - 2.8$ K, depending slightly on gate voltage, in good agreement with the theoretical estimate [35, 37],

$$T_{ES} = 2.8 \left(\frac{1}{4\pi e' \epsilon_0} \right) \left(\frac{e^2}{k_B \xi} \right) \sim 3 \text{ K}. \quad (3)$$

The estimate 3 K is obtained by taking the coherence length, ξ , as the size of the plaquette, $\xi \sim a = 1$ μ m, and

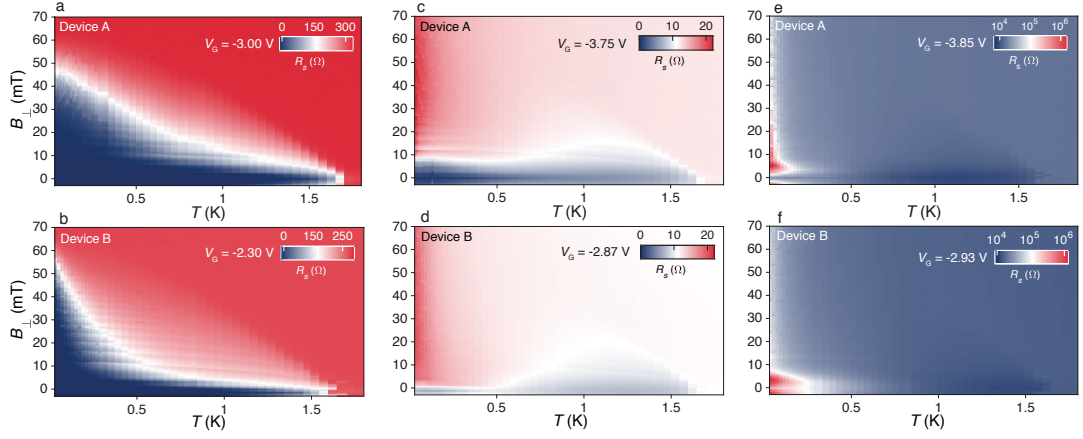


FIG. S2. **Comparing temperature-field planes for two devices** **a-b** Two-dimensional plots of sheet resistance, R_s , as a function of temperature, T , and perpendicular magnetic field, B_\perp for Devices A and B, measured at gate voltages that gave equal normal state resistances in the two devices, spanning the superconducting (S) and anomalous metal (M*) regimes, following labels in Fig. 4(a) of the main text. **c-d** Temperature-field planes for Devices A and B at comparable, moderately negative, gate voltages showing insulating (I), anomalous metal (M*), and normal metal (M) regimes, following the labels in Fig. 4(b) in the main text. **e-f** Temperature-field planes for Devices A and B at comparable, more negative gate voltages, showing insulating (I) regime at low temperature, weakly anomalous metal (M*), and normal metal (M) at higher temperature, following the labels in Fig. 4(c) in the main text.

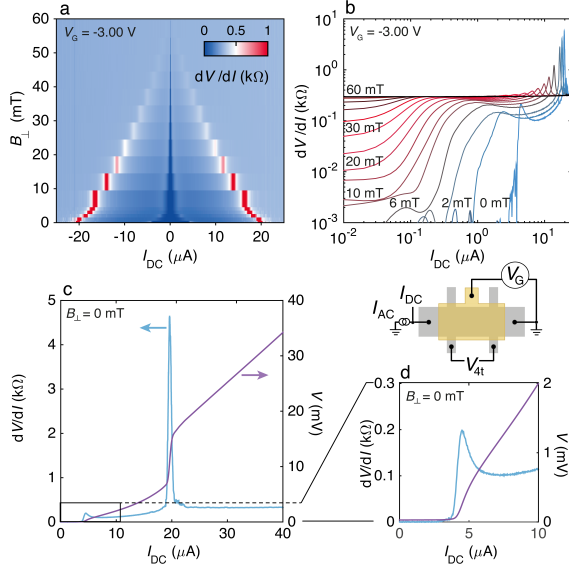


FIG. S3. **Critical currents in superconducting regime.** **a** Differential sheet resistance, dV/dI , as a function of dc current bias, I_{DC} and perpendicular magnetic field, B_\perp , showing two critical currents at $B_\perp = 0$ from global superconductivity to flux-flow to normal. Discrete steps in B_\perp result from coarse spacing of field values. **b** Same data as **a** with log-log scale shows nonzero R_s above $B_\perp \sim 6$ mT. **c** Differential sheet resistance (left axis) and voltage drop per square (right axis) at $B_\perp = 0$, showing two critical currents. **d** Zoom-in on first transition from zero-resistance to low-resistance (flux flow) state. A schematic of the measurement set up is also shown.

the effective dielectric constant $\epsilon' \sim 15$ as the average of InAs ($\epsilon' = 11$) and HfO₂ ($\epsilon' = 18$).

In the activated regime, fits in Fig. S5(b) give $T_0 \sim 1.5$ K. This value is close to the zero-field critical tem-

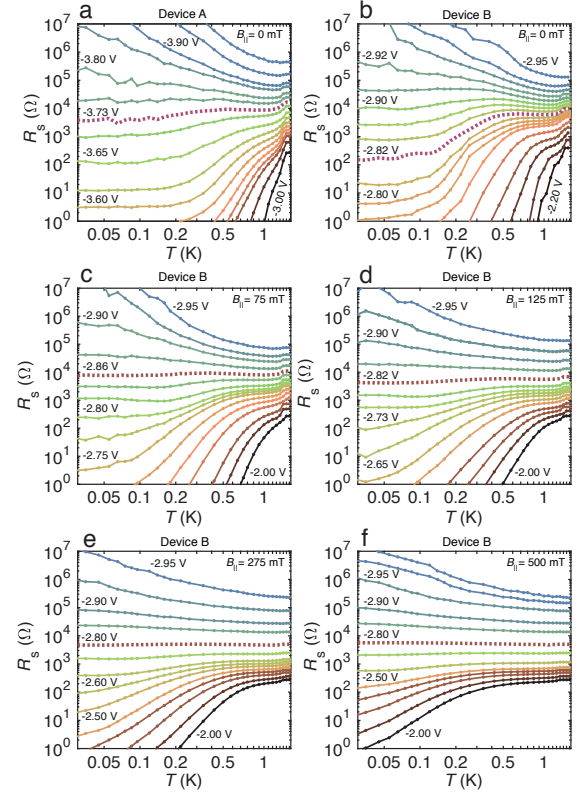


FIG. S4. **In-plane magnetic field effects on SIT transition**

a Temperature evolution of sheet resistance, $R_s(T)$ at $B_\parallel = 0$ for Device A with gate voltages indicated, showing S, M*, and I regimes and separatrix (dashed curve). Points along the curve show measured values. **b** Same as **a**, except for Device B. Note difference in gate voltage range. Separatrix based on flat curve at higher temperature, $T \gtrsim 0.3$ K. **c-e** Sheet resistances, $R_s(T)$, for Device B at in-plane fields $B_\parallel = 75$ mT, 125 mT, 275 mT, and 500 mT shows lowering of the saturation temperature. **f** Sheet resistance, $R_s(T)$, for Device B at in-plane field $B_\parallel = 500$ mT.

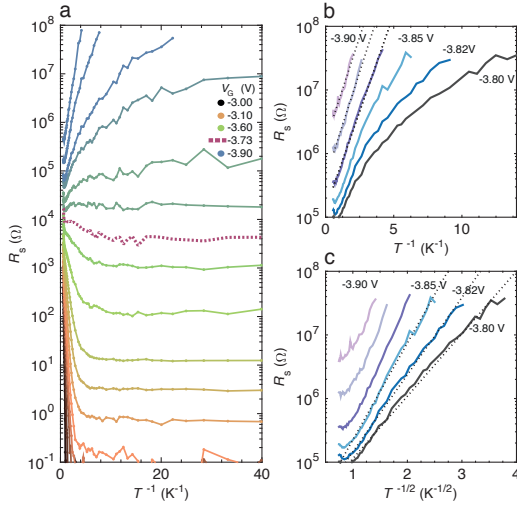


FIG. S5. Activated transport and variable-range hopping. **a** Same data as Fig. 2(a) versus inverse temperature with log-log axes. **b**, Same data as **a**, with a linear horizontal axis. A straight line on this plot indicates activated transport, $R(T) \propto \exp(T_0/T)$. Line fit to most negative gate voltages (dashed lines) yield $T_0 = 1.5$ K. **c** Same data as **b**, plotted versus $T^{-1/2}$. Efros-Shklovskii variable range hopping (ES-VRH), $R(T) \propto \exp(T_1/T)^{1/2}$ appears as a straight line. The three bottom data sets (dashed lines) yield $T_1 = 2.3$ K, 2.5 K, 2.8 K for $V_G = -3.80$ V, -3.82 V, -3.85 V.

perature, $T_c \sim 1.6$ K. The similarity of values for T_0 and T_c was noted previously in amorphous InO films [38]. Previous studies on disordered TiN films [36] showed a crossover from activated transport to ES-VRH as the temperature was increased, not as a function of disorder. Values for T_1 in [36] were similar to the values found here, while values for T_0 were three to five times smaller than found here.